J Mater Sci (2011) 46:4176–4190
DOI 10.1007/s10853-011-5352-8

IIB 2010

Impurity and vacancy segregation at symmetric tilt grain boundaries in Y_2O_3-doped ZrO_2

Masato Yoshiya · Takashi Oyama

Received: 6 October 2010 / Accepted: 31 January 2011 / Published online: 15 February 2011

Abstract Segregation energies of impurity ions and oxygen vacancies at grain boundaries in Y_2O_3-doped ZrO_2 as calculated from atomistic simulations using energy minimization and Monte Carlo methods are reported. Based on these energies, local defect equilibrium concentrations have been estimated. It is found that it is more energetically favorable for an yttrium ion to be accompanied by an oxygen vacancy at grain boundaries, although decrease in energy when associated with an oxygen vacancy differs from boundary to boundary. The segregation energy for a neutral defect complex consisting of a two yttrium ions and an oxygen vacancy at infinitely dilute concentration is highly correlated with the coordination environment of each site in the vicinity of the grain boundary (GB), and, in turn, GB energy. Although the estimated local equilibrium concentrations of these defects are similar, detailed analysis of the atomic coordination and defect distributions in the vicinity of a GB reveal that defect distributions, especially of oxygen vacancies, are dependent on the characteristics of the particular GB and that segregation in effect reduces lattice strains at the GB. Equilibrium concentration distributions of yttrium at grain boundaries are also given as a function of spatial resolution, and are useful for interpretation of experimental results.

M. Yoshiya · T. Oyama
Nanostructure Research Laboratory, Japan Fine Ceramics Center, 2-4-1 Mutsuno, Atsuta, Nagoya 456-8587, Japan

M. Yoshiya (✉)
Department of Adaptive Machine Systems, Osaka University, 2-1 Yamadaoka, Suita, Osaka 565-0871, Japan
e-mail: yoshiya@ams.eng.osaka-u.ac.jp

T. Oyama
Murata Manufacturing Co., Ltd., 1-10-1, Higashikotari, Nagaokakyo, Kyoto 617-8555, Japan

Introduction

Changes in atomic coordination environments relative to the bulk crystal occur not only within adjoining planes at a grain boundary (GB), but often also several crystal layers either side of a boundary. This has been observed directly using high resolution transmission electron microscopy and scanning transmission electron microscopy (STEM) in numerous oxide systems. The distortion of the crystal lattice in the vicinity of GBs brings about changes in chemical bonding between the atoms, and thus energies for various point defects, including impurities and vacancies, will differ from those in the bulk, providing a driving force for enrichment or depletion of these point defects at GBs, i.e., GB segregation.

GB segregation has been known for a long time, and typically has a detrimental effect on the properties of polycrystalline materials, e.g., segregation of sulfur to GBs in steel. However, there are some materials properties that are believed to originate from GB segregation which are intentionally utilized in many practical devices.

Hondros and Seah reported an empirical relationship between solubility in the bulk and the magnitude of GB segregation [1], which aids our understanding of GB segregation from a phenomenological viewpoint. However, the underlying physics that govern GB segregation are still not well understood, which is an impediment to the tailoring of GBs to exhibit new properties. On the other hand, theoretical models based on macroscopic thermodynamics and statistical mechanics, including the Langmuir–McLean and BET models [2–4], have contributed to quantitative analysis of GB segregation. These require explicit determination of interactions between GB and defects, including those between impurities and vacancies, so that atomic-level calculations are essential.

ZrO_2-based materials are one of the most extensively studied systems with regard to fundamental understanding of GBs in oxides and practical applications. They exhibit the fluorite crystal structure when doped with a small amount of aliovalent oxide. Since the cation sublattice has FCC symmetry, it can be directly compared with the structure of FCC metals, making this oxide suitable for fundamental investigations.

When Y_2O_3 is added to ZrO_2, two kinds of point defects with oppositely signed effective charges, Y'_{Zr} and $V_O^{\bullet\bullet}$ in Kröger–Vink notation, are produced:

$$Y_2O_3 \rightarrow 2Y'_{Zr} + V_O^{\bullet\bullet} + 3O_O^{\times} \tag{1}$$

In this case impurity segregation at GBs involves movement of Y'_{Zr}, $V_O^{\bullet\bullet}$ or both.

Local atomic environments at various GBs have been revealed by STEM [5–10], with GB segregation of impurities identified on the nanometer level [5, 6, 11]. However, these techniques are unable to determine the distribution of segregating ions and vacancies in three dimensions; the spatial resolution of energy-dispersive X-ray spectroscopy (EDX) and electron energy-loss spectroscopy (EELS) are also not high enough to identify which specific site an impurity occupies, a situation exacerbated if there is only a small difference in atomic number between matrix and dopant, as is the case with Zr and Y. Furthermore, O columns tend to be distorted in the vicinity of GBs and thus it is quite difficult to determine whether the change in intensity is due to distortion of the O column or presence of vacancies. In contrast, atomic-level simulations enable the prediction of the three-dimensional distribution of Y'_{Zr} and $V_O^{\bullet\bullet}$, providing a detailed understanding of the phenomenon of GB segregation and its impact on properties such as ionic conduction across or parallel to the GB.

Because of their high oxide ion conductivity, zirconia materials are prime candidates for use as electrodes [12] and solid-state electrolytes [13] for solid oxide fuel cells [14], as well as oxygen gas sensors [15]. It is widely known that ionic conductivity at GBs is typically at least a few orders of magnitude smaller because of the higher activation energy for oxide ion migration than in the grain interior [16–21], resulting in lower overall ionic conductivity in polycrystalline materials than in a single crystal. This so-called GB resistance is in many cases attributed to GB segregation. At the same time, GB segregation [22–27] and surface segregation [28–38] in Y_2O_3-doped ZrO_2 have been directly or indirectly studied by experiment and computation. We note that under equilibrium conditions, the degree of segregation is practically independent of crystal structure, i.e., whether cubic or tetragonal [34].

To examine the GB resistance caused by segregation, Guo applied the space-charge theory to GBs in ZrO_2-based materials [39], and this has been followed by many other studies using the space-charge model to explain the observed phenomena [39–44]. According to this model, Y'_{Zr} is enriched at the GB core and $V_O^{\bullet\bullet}$ is depleted in the vicinity of the GB, gradually assuming bulk concentration values as the distance from the GB increases. Although this model has been assumed adequate to explain the effect of segregation, there are two important points to note: (a) Enrichment of Y'_{Zr} is a prerequisite of this theory, with no explanation or mechanism given for why it occurs, and (b) no account is taken of the specific GB structure or variation in coordination environments vis-à-vis the bulk. With regard to (a), although it is reasonable to assume Y'_{Zr} enrichment occurs at GB cores since it has been frequently observed experimentally, segregation of oxide ion vacancies is practically impossible to detect, so there is no direct evidence for its occurrence. Nevertheless, in a previous simulation study [25], we found that segregation of isolated yttrium ions is energetically unfavorable, and co-segregation with oxygen vacancies is needed to relieve the local strain imposed by yttrium ions at a GB. With regard to (b), it is essential to take the specific atomic arrangements into account when determining the dependence of GB or surface segregation on crystallographic orientation [17, 33]. Given the difficulty of carrying out such characterization experimentally, computational studies of GB segregation on the atomic level are required to fully understand this phenomenon.

On the other hand, Mondal et al. reported one to two orders of magnitude higher ionic conductivity in nanocrystals than in microcrystals, assuming that GB conductivity is independent of grain size and GB conductance decreases with grain size [45]. Knöner et al. [46] reported three orders of magnitude higher ionic conductivity at GBs of nanocrystals than in a single crystal, although their assumptions that ionic conductivity remains unchanged even when the bulk composition is changed, and that the GB width in their system is that same as that reported in the literature are questionable. Similar increases in ionic conductivity for 15 nm thick Y_2O_3-doped ZrO_2 textured thin films on MgO substrates have been reported by Kosacki et al., who estimated the interface layer to be 1.6 nm thick [47, 48].

Recently, Garcia-Barriocanal et al. reported eight orders of magnitude higher ionic conductivity in Y_2O_3-doped ZrO_2 thin films sandwiched between $SrTiO_3$ layers [49]. They attributed this colossal increase in ionic conductivity to the lower activation energy associated with disordered oxygen ions at YSZ/STO interfaces caused by the large lattice strain (7%), as long as the interface remained coherent. However, according to theoretical calculations by Kushima et al. [50], this interface effect is not sufficient to account for the increase in ionic conductivity. The origin of the increased conductivity thus remains unclear. The dearth of understanding of the effect of changes in atomic coordination, composition and energetics at GBs and heterointerfaces on macroscopic properties needs to be remedied if materials are to be designed successfully on the nanoscale.

In our previous study [25], we carried out numerical analyses based on atomistic simulation of GB segregation at a Σ5 (310)/[001] GB. It was found that Y'_{Zr} segregation to GBs must be accompanied by vacancy segregation. The driving force for the segregation is the release of local strain imposed by the large Y ions. The equilibrium local concentrations of Y'_{Zr} and $V_O^{\bullet\bullet}$ species were calculated by comparing the energies of various configurations of dopants and vacancies in the GB region or grain interior, and the results found to be in good agreement with experiment. Monte Carlo simulations of site exchange in combination with static lattice calculations verified these findings.

The previous study was confined to a specific GB and thus it is unclear whether the above findings apply to other GBs. Therefore, in this study, systematic atomistic simulations were carried out for five symmetric tilt GBs, in coincidence site lattice (CSL) notation namely Σ5 (210)/[001], Σ5 (310)/[001], Σ13 (510)/[001], Σ11(113)/[011], and Σ9 (221)/[011], in order to determine the generality of the findings from the previous study and their dependence on individual GB characteristics.

This paper is composed as follows: In the next section, the computational procedures used are outlined, followed by results for the five GBs in pure cubic ZrO_2. In "Dopant segregation and coordination environments" section, we report results obtained for infinitely dilute concentrations of Y'_{Zr} and $V_O^{\bullet\bullet}$, focusing on whether $V_O^{\bullet\bullet}$ is needed for Y'_{Zr} segregation. Next, from results of calculations at higher concentrations of these defects, the equilibrium local defect concentration at each GB is evaluated in order to determine if there is any dependence on crystallographic orientation or GB structure. Finally, line profiles of defect concentrations across each GB are given for comparison with experimental findings.

Methodology

Static lattice calculations

The most stable atomic configuration for a given orientation relationship between neighboring grains and Y_2O_3 content in the vicinity of each GB was computed by the static lattice energy minimization technique using empirical interatomic potentials. The GB energy, γ, was then calculated as

$$\gamma = (E_{GB} - n \cdot E_{ZrO_2})/2A \tag{2}$$

where E_{GB} is the total energy of a supercell containing two GBs, n is the number of unit cells that together give the same number of atoms as in the GB-containing supercell, E_{ZrO_2} is the total energy of a ZrO_2 unit cell, and A is the area of each GB plane bounded by the supercell. When the supercell contains yttrium and vacancies, the lattice energy of a Y_2O_3 unit multiplied by the number of unit cells equivalent to the Y_2O_3 concentration must also be subtracted to calculate the GB energy. For any system, the total energy of a supercell or a unit cell, E_{total}, was simply calculated as the sum of interatomic pair potentials of the Born–Mayer–Huggins form:

$$E^{total} = \frac{1}{2}\sum_i \sum_{j \neq i} \left(A_{ij} \exp\left(-\frac{r_{ij}}{\rho_{ij}} \right) - \frac{C_{ij}}{r_{ij}^6} + \frac{q_i q_j}{r_{ij}} \right) \tag{3}$$

where r_{ij} is the distance between ions i and j, q_i is the charge of ion i, and A_{ij}, ρ_{ij}, and C_{ij} are potential parameters specific to each pair of ionic species. In this study, highly transferrable potential parameters reported in the literature for Zr^{4+}–O^{2-} [51], Y^{3+}–O^{2-} [52], and O^{2-}–O^{2-} [52] were used. Although this combination of potential parameters does not reproduce the cubic-to-tetragonal phase transition upon decreasing temperature or decreasing Y_2O_3 content, it is not crucial since Y_2O_3 is enriched at the GB and therefore it is reasonable to assume that the cubic structure will be stabilized in its vicinity. The short-range interatomic potentials were truncated at 2.0 nm during structural optimization, and the same cutoff was used in Ewald summation of the Coulombic terms. In the case of Monte Carlo simulations, a cutoff of 0.8 nm was used. The shorter cutoff of 0.8 nm was chosen to reduce the computational time, as a huge number of different configurations had to be considered for each Y_2O_3 content. The structural optimization of the final structure from the Monte Carlo simulations was carried out using the longer cutoff.

The excess volume, V_{excess}, of a GB was defined in this study as

$$V_{excess} = (V_{GB} - V_{bulk})/2A \tag{4}$$

where V_{GB} is the volume of a supercell containing two GBs and V_{bulk} is the volume of a supercell of a single crystal containing the same number of ions as in the GB model. Since the excess volume is calculated per unit area of a GB to enable comparison between different GB models, it is equal to half the increase in length of the supercell when two GBs are added to the system. All the calculations were performed using the GULP code [53]. Further details of the static lattice method are given elsewhere [25].

Monte Carlo simulation of site interchange

Although O ions are mobile at elevated temperature in Y_2O_3-doped ZrO_2, the diffusivity of cations is many orders of magnitude lower, which makes it impractical to calculate reliable cation diffusion coefficients by molecular dynamics within a reasonable timescale. To overcome this limitation, Monte Carlo simulations involving site interchange of both anions and cations were carried out.

Monte Carlo simulations were carried out to efficiently sample the phase space by trialing exchanges of Y'_{Zr} and $V_O^{\bullet\bullet}$ species with Zr and O species, respectively, on randomly chosen nearest neighbor sites. The energy change, ΔE_{total}, for each exchange trial was calculated using the energies calculated by the static lattice method for the configuration before and after the exchange. The acceptance ratio, R_a, for each trial was calculated according to the Metropolis method [54] as

$$R_a = \begin{cases} 1 & (\Delta E_{total} < 0) \\ \exp(-\Delta E_{total}/k_B T) & (\Delta E_{total} \geq 0) \end{cases} \tag{5}$$

where k_B is the Boltzmann constant and T is temperature, set at 300 K to allow small thermal fluctuations to provide sufficient energy for the structure to escape from shallow local minima. When ΔE_{total} was negative, the exchange was always accepted, but when ΔE_{total} was positive, the exchange was accepted only if a randomly chosen number between 0 and 1 was greater than R_a.

For each trial, two yttrium ions were exchanged with two randomly chosen zirconium ions and one oxygen ion was exchanged with $V_O^{\bullet\bullet}$ at random. This process was repeated until the total energy of the supercell converged to within the magnitude of the thermal fluctuations at 300 K.

The GB region was defined as those atoms within a box centered on the GB plane and extending 1.0 nm either side of the GB plane or bounded by the supercell parallel to the GB, as illustrated in Fig. 1. The value of 1.0 nm was chosen because beyond this distance the energies of point defects are the same as those in the bulk crystal, as will be discussed in "Dopant segregation and coordination environments" section. Increasing the GB region simply results in increased computational time and does not affect the results obtained. In this way, total energies and equilibrium atomic configurations for a given local Y_2O_3 concentration at each GB were obtained, and chemical potentials calculated as the first derivative of the total energy with respect to Y_2O_3 content.

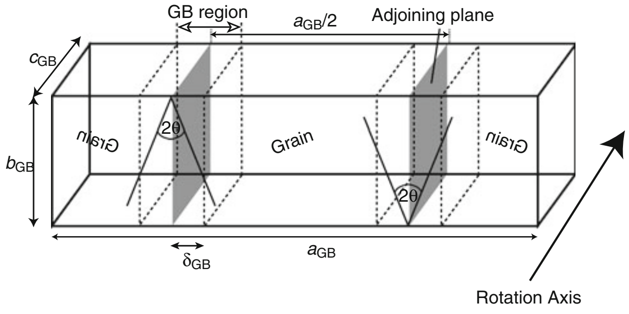

Fig. 1 Schematic illustration of a GB simulation supercell. Three-dimensional periodic boundary conditions result in two identical GBs (indicated by *gray planes*) being formed. In this study the GB region is defined as the section of crystal 1.0 nm either side of a GB plane

Grain boundary models

When two grains of different orientation join to form a GB, the structure in the vicinity of the GB becomes distorted, with different atom arrangements and coordination environments than in the grain interior. Five symmetric tilt GBs, Σ5 (210)/[001], Σ5 (310)/[001], Σ13 (510)/[001], Σ9 (122)/[011], and Σ11(311)/[011] GBs, were examined in this study. The structures of these GBs have previously been examined by STEM and thus can be directly compared with our computational results. The rotation axis of the first three GBs is [001], and the corresponding surface planes, namely (210), (310), and (510) planes, respectively, are all non-polar. In contrast, the rotation axis of the last two GBs is [011], and the corresponding surfaces terminated at (122) and (311) planes, respectively, are polar, which makes the construction and calculation of GB-containing supercells more complex, as will be discussed in the following sections.

General features of the supercells for the five GBs are summarized in Fig. 1. Each supercell is longest in the direction perpendicular to the GB plane, and each contains two equivalent GBs so that three-dimensional periodic boundary conditions can be applied. Preliminary calculations in which the inter-GB distance was varied indicated beyond 3.0 nm the interaction between the two GBs is negligibly small, so this was the minimum inter-GB distance used when constructing the supercells. In the case of the Σ13 (510)/[001] GB, distortion of atom columns occurs over wider region either side of the GB plane. Thus, a longer supercell was used for that GB. The widths of the five GB supercells, b_{GB}, were $\sqrt{5}\cdot a_{unit}$, $\sqrt{10}/2\cdot a_{unit}$, $\sqrt{26}/2\cdot a_{unit}$, $\sqrt{22}/2\cdot a_{unit}$ and $\sqrt{18}/2\cdot a_{unit}$ for Σ5 (210)/[001], Σ5 (310)/[001], Σ13 (510)/[001], Σ9 (221)/[011], and Σ11(113)/[011] GBs, respectively, where a_{unit} is the lattice constant of cubic ZrO_2, calculated to be 0.512 nm in this study. The depths of GBs with [001] and [011] rotation axes, c_{GB}, were $2a_{unit}$ and $\sqrt{2}a_{unit}$ respectively. Although the widths and depths of the supercells are rather small, any interactions between a defect and its images in neighboring cells remained almost unchanged even in the vicinity of GBs when the segregation energy relative to the bulk one was calculated, as the same interactions were experienced by defects in the grain interior. Although this is not always true for other materials or geometries, preliminary calculations using the GB-containing supercell with twice the width and depth as those in the original supercell showed negligibly small differences in the segregation energy calculated by Eq. 6. Thus, the segregation energies plotted in Figs. 3, 4, and 5 represent those for the defect at infinitely dilute concentration.

Supercells of all five GBs for pure ZrO_2 are shown in Fig. 2, where the size of the cubic ZrO_2 unit cell is indicated by dotted lines at the center of each supercell. The tilt angles, θ, of grains at these GBs are 26.6°, 18.4°, 11.3°, 70.5°, and 19.5°, respectively, where 2θ gives the misorientation angle between the two grains. These atomic configurations yielded the lowest GB energy for each misorientation based on calculations in which various microscopic degrees of freedom, including rigid-body translation (RBT), were surveyed. Shibata et al. carried out preliminary calculations for (221)/[001] and (113)/[011] GBs of ZrO_2 to aid interpretation of their HAADF-STEM images [9]. They succeeded in determining the optimum RBT, although the precise positions of O ions, which are hard to detect by HAADF-STEM because of their small Z value, are still unclear. Based on the positions of Zr ions

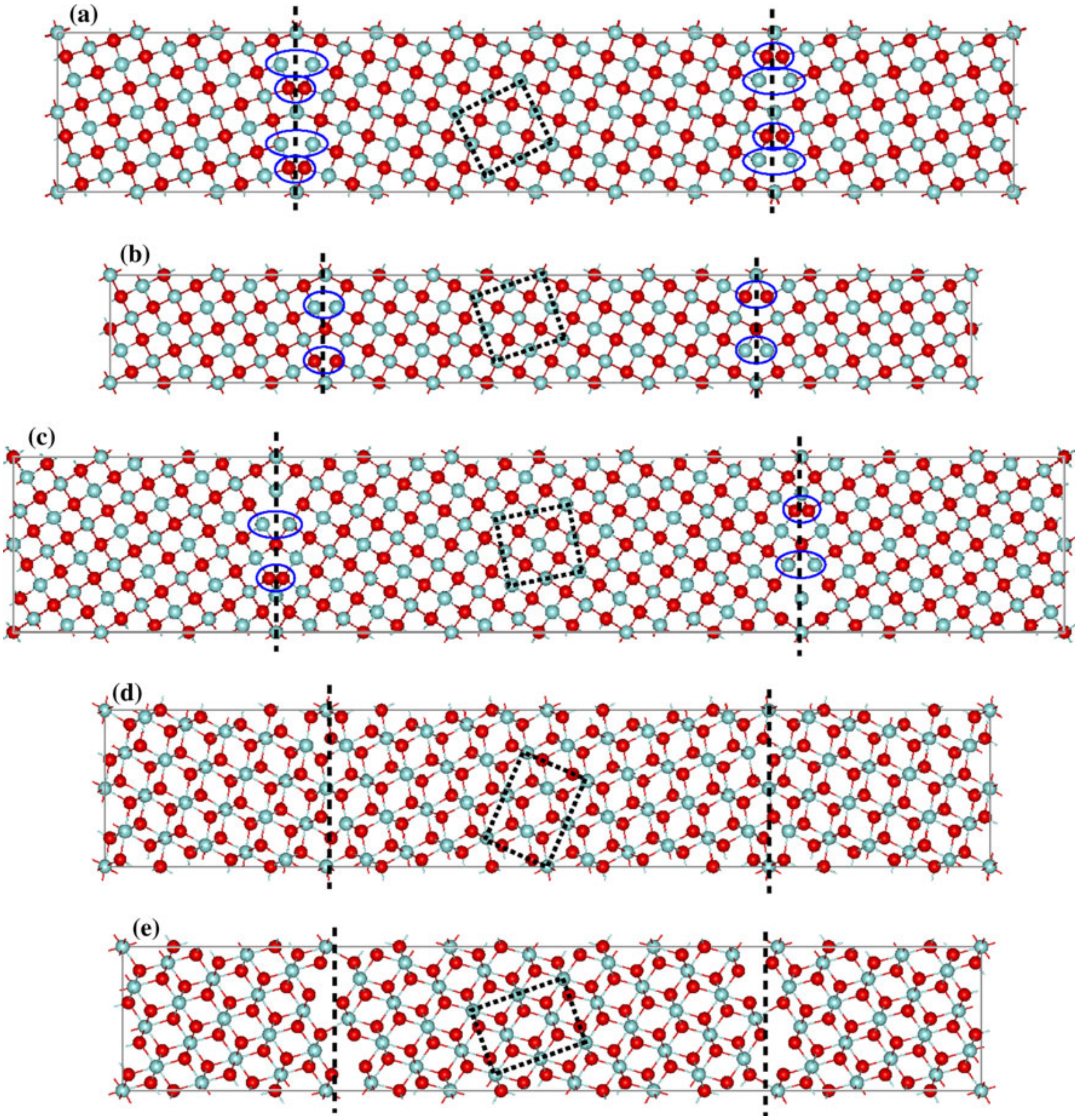

Fig. 2 Initial structures for GB-containing supercells for **a** Σ5 (210)/[001], **b** Σ5 (310)/[001], **c** Σ13 (510)/[001], **d** Σ11(113)/[011], and **e** Σ9 (221)/[011] GBs projected onto a two-dimensional plane perpendicular to the GB plane. *Light blue balls* and *red balls* (*light gray balls* and *dark gray balls* in *gray scale*) represent Zr and O atoms, respectively (Color figure online)

Table 1 Properties of the five pure ZrO_2 grain boundaries examined in this study

Grain boundary	Inclination angle (°)	GB energy (J/m^2)	Excess volume (nm)
Σ5 (210)/[001]	26.6	2.69	0.11
Σ5 (310)/[001]	18.4	2.52	0.08
Σ13 (510)/[001]	11.3	2.64	0.10
Σ11 (113)/[011]	70.5	2.78	0.08
Σ9 (221)/[011]	19.5	1.37	0.04

they reported, we have carried out further calculations to determine the positions of O ions at these GBs.

GBs with a [001] rotation axis exhibit mirror symmetry about the GB plane, similar to GBs of FCC Al [55], since like planes face each other across the interface, i.e., they form symmetric tilt GBs. As a result, ions with the same charge sign are proximate to each other across the GB planes. In order to reduce Coulombic repulsion between cations or anions, the pairs of atomic columns in Fig. 2 within the blue ellipses have only half the atom density of other columns, with atoms facing vacancies across the interface in a zigzag manner along the c_{GB} direction [25]. Although some of these half-occupied columns remain separate after structural optimization in the case of pure ZrO_2, they eventually merge to form one fully occupied column upon GB segregation of Y_2O_3 in the case of the Σ5 (310)/[001] GB [25], in good agreement with experiment. Y_2O_3 segregation must therefore be taken into account to reproduce experimentally observed GB structures [25]. In contrast, in the case of GBs with a [011] rotation axis, RBT yielded stable atomic configurations at the GB cores since it enables cations to be positioned next to anions across polar GB planes, optimizing the coordination environments of atoms at the GB core.

Properties of the five GBs calculated for pure ZrO_2 are summarized in Table 1. All have moderate GB energies and excess volumes. We note that the three GBs with a [001] rotation axis are similar in GB energy, even though the atoms in the vicinity of each GB have different coordinations on account of the wide range of their misorientation angles.

Dopant segregation and coordination environments

Calculations for infinite dilute concentrations of dopants were carried out to examine the factors that govern GB segregation of yttrium and oxygen vacancies. For each GB system, a point defect, Y'_{Zr} or $V_O^{\bullet\bullet}$, or a defect complex, $\left(Y'_{Zr}\cdot V_O^{\bullet\bullet}\right)^{\bullet}$ or $\left(2Y'_{Zr}\cdot V_O^{\bullet\bullet}\right)^{\times}$, was placed at various distances from the GB plane. All atomic coordinates in the supercell, in addition to the supercell volume, were relaxed to minimum energy to determine the energy change associated with the point defect or the defect complex as a function of distance from the GB plane relative to its energy in the bulk. The segregation energy, $E_{seg}(r)$, of a defect or defect complex was defined in this study as

$$E_{seg}(r) = E_{total}(r) - E_{total}(\infty) \qquad (6)$$

where r is the distance of the defect or complex from the GB plane, and $E_{total}(r)$ is the total energy of the defect-containing supercell. $E_{total}(\infty)$ represents the total energy of the supercell when the defect or defect complex is located at the middle of a grain (crystal bulk). For better accuracy, a number of values for supercells with the defect at different positions at the center of a grain were averaged to give $E_{total}(\infty)$. In the case of defect complexes, a $V_O^{\bullet\bullet}$ was placed at the second nearest neighbor site to the Y'_{Zr} species at close to the same r as for Y'_{Zr}; the relative coordinates of the defect complexes were kept the same for calculations at different distances from the GB plane. Similarly, although the dimensions of each supercell parallel to the GB plane are different, as can be seen from Fig. 2, the segregation energies evaluated in the above manner are practically independent of the supercell size in this study for the reasons given above.

Figure 3 shows segregation energies of defects and a defect complex for the five GBs as a function of distance from the respective GB planes. First, for the Σ5 (310)/[001] GB, the Y'_{Zr} segregation energy increased as shown in Fig. 3b, while the $\left(Y'_{Zr}\cdot V_O^{\bullet\bullet}\right)^{\bullet}$ segregation energy decreased as the distance from the GB plane decreased, although there is some scatter in the values closer to the GB plane. Thus, isolated segregation of a Y'_{Zr} dopant is energetically unfavorable, while it is favorable when the dopant is accompanied by a $V_O^{\bullet\bullet}$. Detailed analysis revealed that the local strain imposed by an Y ion, which is larger than a Zr ion, is relieved by the presence of a $V_O^{\bullet\bullet}$ at the GB, and this strain release is the driving force for co-segregation of Y'_{Zr} and $V_O^{\bullet\bullet}$, and not the Coulombic interaction between them and other defects at the GB. When the space-charge theory is applied to the ZrO_2–Y_2O_3 system [39], segregation of Y'_{Zr} is assumed to be a prerequisite for $V_O^{\bullet\bullet}$ depletion, perhaps because Y'_{Zr} segregation is often observed experimentally. According to our calculations for the Σ5 (310)/[001] GB, however, Y'_{Zr} needs to be accompanied by $V_O^{\bullet\bullet}$ for GB segregation to occur. The same result was found in our previous study of the Σ5 (310)/[001] GB in which the GB region either side of the interface was taken as 0.6 nm [25] as compared to 1.0 nm in this study. This indicates that beyond a certain width the size of the GB region does not significantly affect the results. The same can be said for the other GBs examined in this study

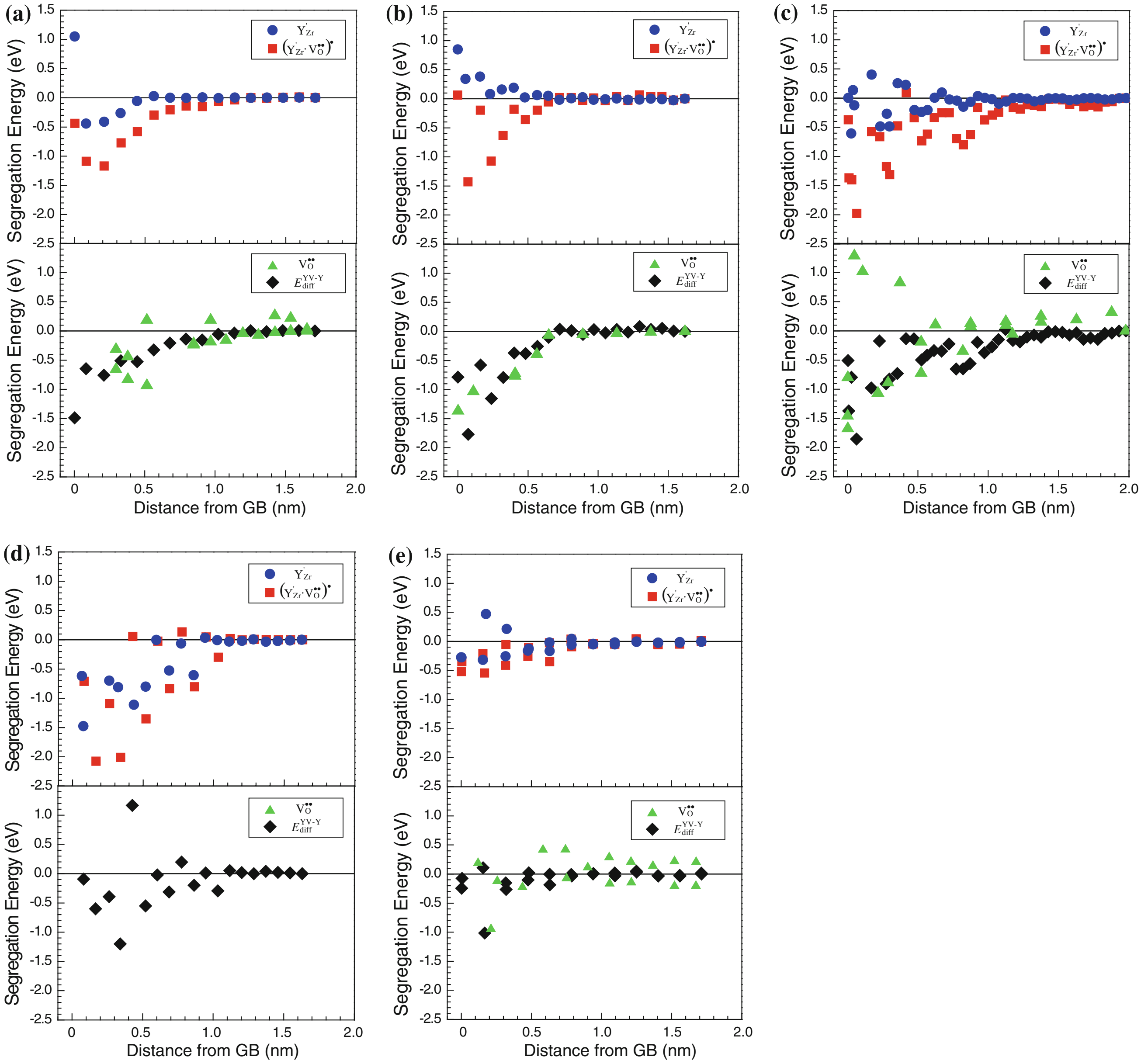

Fig. 3 Segregation energies of a Y'_{Zr} species (*blue circles*) and a $\left(2Y'_{Zr}\cdot V_{O}^{\bullet\bullet}\right)^{\times}$ pair (*red squares*) (*upper half*) and segregation energies of a $V_{O}^{\bullet\bullet}$ (*green triangles*) species and the energy difference between isolated and bound pairs, E_{diff}^{YV-Y}, (*black squares*) (*lower half*) as a function of distance from the GB plane for **a** Σ5 (210)/[001], **b** Σ5 (310)/[001], **c** Σ13 (510)/[001], **d** Σ11(113)/[011], and **e** Σ9 (221)/[011] GBs (Color figure online)

making it possible to compare their segregation energies assuming a fixed GB region size regardless of the degree of misorientation.

Calculation of segregation energies for $V_{O}^{\bullet\bullet}$ by the static lattice method is at times more difficult than those for Y'_{Zr} and $\left(Y'_{Zr}\cdot V_{O}^{\bullet\bullet}\right)^{\bullet}$ defects because neighboring oxygens can easily move onto the vacant sites. If $V_{O}^{\bullet\bullet}$ simply moves to another site of the O sublattice, the obtained result is valid for the settled site. However, when the position of the $V_{O}^{\bullet\bullet}$ deviates significantly from the ideal O sublattice, it is more difficult to interpret. Because of this, when the position of the oxygen vacancy changed by more than 0.01 nm from its original position upon structural optimization, the data point was excluded from the plot of segregation energy versus distance. We note that this does not change the overall trends at all, but simply reduces the number of data points in any given plot. For the same reason, the number of data points for the interaction energy between Y'_{Zr} and $V_{O}^{\bullet\bullet}$, i.e., $E_{interact}^{Y-V}$, was limited to those for which reliable $V_{O}^{\bullet\bullet}$ data points were found, since $E_{interact}^{Y-V}$ is defined as

$$E_{\mathrm{interact}}^{\mathrm{Y-V}} = E_{\mathrm{seg}}^{\mathrm{YV}} - \left(E_{\mathrm{seg}}^{\mathrm{Y}} + E_{\mathrm{seg}}^{\mathrm{V}}\right) \tag{7}$$

where $E_{\mathrm{seg}}^{\mathrm{YV}}$, $E_{\mathrm{seg}}^{\mathrm{Y}}$, and $E_{\mathrm{seg}}^{\mathrm{V}}$ are segregation energies of $\left(\mathrm{Y}_{\mathrm{Zr}}' \cdot \mathrm{V}_{\mathrm{O}}^{\bullet\bullet}\right)^{\bullet}$, $\mathrm{Y}_{\mathrm{Zr}}'$, and $\mathrm{V}_{\mathrm{O}}^{\bullet\bullet}$, respectively. Instead of directly evaluating $E_{\mathrm{interact}}^{\mathrm{Y-V}}$, to improve the statistical accuracy the energy difference between segregation energies of $\left(\mathrm{Y}_{\mathrm{Zr}}' \cdot \mathrm{V}_{\mathrm{O}}^{\bullet\bullet}\right)^{\bullet}$ and $\mathrm{Y}_{\mathrm{Zr}}'$, $E_{\mathrm{diff}}^{\mathrm{YV-Y}}$ was calculated as

$$E_{\mathrm{diff}}^{\mathrm{YV-Y}} = E_{\mathrm{seg}}^{\mathrm{YV}} - E_{\mathrm{seg}}^{\mathrm{Y}}. \tag{8}$$

This is because the number of data points for $E_{\mathrm{diff}}^{\mathrm{YV-Y}}$ is the same as those for $E_{\mathrm{seg}}^{\mathrm{Y}}$ and $E_{\mathrm{seg}}^{\mathrm{YV}}$, and many more than those for $E_{\mathrm{seg}}^{\mathrm{V}}$. Plots of $E_{\mathrm{diff}}^{\mathrm{YV-Y}}$ versus distance can thus be directly compared with $E_{\mathrm{seg}}^{\mathrm{V}}$: If $E_{\mathrm{diff}}^{\mathrm{YV-Y}}$ is smaller than $E_{\mathrm{seg}}^{\mathrm{V}}$, it indicates binding between $\mathrm{Y}_{\mathrm{Zr}}'$ and $\mathrm{V}_{\mathrm{O}}^{\bullet\bullet}$ is more energetically favorable than the vacancies remaining in the grain interior, and thus segregation of $\mathrm{V}_{\mathrm{O}}^{\bullet\bullet}$ with $\mathrm{Y}_{\mathrm{Zr}}'$ to the GB is favored. If $E_{\mathrm{diff}}^{\mathrm{YV-Y}}$ is larger than $E_{\mathrm{seg}}^{\mathrm{V}}$, then $\mathrm{Y}_{\mathrm{Zr}}'$ and $\mathrm{V}_{\mathrm{O}}^{\bullet\bullet}$ repel each other upon segregation.

In the lower half of Fig. 3b, the segregation energy of a $\mathrm{V}_{\mathrm{O}}^{\bullet\bullet}$ is shown as a function of distance from the GB plane together with $E_{\mathrm{diff}}^{\mathrm{YV-Y}}$. The segregation energy of $\mathrm{V}_{\mathrm{O}}^{\bullet\bullet}$ decreased monotonically upon approaching the GB plane. This indicates that $\mathrm{V}_{\mathrm{O}}^{\bullet\bullet}$ will spontaneously segregate to the GB region. This also contradicts the assumption made in the space-charge theory [39].

$E_{\mathrm{diff}}^{\mathrm{YV-Y}}$ also decreases monotonically upon approaching the GB plane. Even the few specific sites that resulted in positive and higher segregation energies for $\mathrm{Y}_{\mathrm{Zr}}'$ yielded negative values of $E_{\mathrm{diff}}^{\mathrm{YV-Y}}$. From the crystal bulk up to a distance of 0.6 nm from the interface, $E_{\mathrm{seg}}^{\mathrm{V}}$ is similar to $E_{\mathrm{diff}}^{\mathrm{YV-Y}}$. At 0.4 nm from the interface, it becomes smaller than $E_{\mathrm{diff}}^{\mathrm{YV-Y}}$, while at distances under 0.3 nm $E_{\mathrm{diff}}^{\mathrm{YV-Y}}$ is smaller than $E_{\mathrm{seg}}^{\mathrm{V}}$. This shows that segregation of $\mathrm{Y}_{\mathrm{Zr}}'$ results in increased $\mathrm{V}_{\mathrm{O}}^{\bullet\bullet}$ concentration near the GB core. Thus, $\mathrm{V}_{\mathrm{O}}^{\bullet\bullet}$ should be enriched at this GB, instead of, as argued in space-charge theory, depleted [39]. This is quantitatively confirmed for the first time with this additional calculations for $\mathrm{V}_{\mathrm{O}}^{\bullet\bullet}$ in this study.

The segregation energy of $\mathrm{Y}_{\mathrm{Zr}}'$ decreased below zero upon approaching the GB plane of the Σ5 (210)/[001] GB except on the GB plane itself ($r = 0$), although the decrease in the segregation energy is modest, as seen in Fig. 3a. This indicates $\mathrm{Y}_{\mathrm{Zr}}'$ can segregate even without $\mathrm{V}_{\mathrm{O}}^{\bullet\bullet}$ at this GB. As for $\left(\mathrm{Y}_{\mathrm{Zr}}' \cdot \mathrm{V}_{\mathrm{O}}^{\bullet\bullet}\right)^{\bullet}$ complexes, the segregation energy decreased upon approaching the GB plane more rapidly than for $\mathrm{Y}_{\mathrm{Zr}}'$, implying that GB segregation of $\mathrm{Y}_{\mathrm{Zr}}'$ is more favorable when $\mathrm{Y}_{\mathrm{Zr}}'$ is accompanied by $\mathrm{V}_{\mathrm{O}}^{\bullet\bullet}$. There are gaps in the $\mathrm{V}_{\mathrm{O}}^{\bullet\bullet}$ segregation energies especially near the GB core and $r = 0.7$ nm because of the movement of oxygen vacancies as mentioned earlier. The configurational changes upon structural optimization by the static lattice method imply that $\mathrm{V}_{\mathrm{O}}^{\bullet\bullet}$ is unstable at those positions relative to neighboring sites. Nevertheless, the data suggests that $\mathrm{V}_{\mathrm{O}}^{\bullet\bullet}$ is not as strongly segregated to this GB as the Σ5 (310)/[001] GB. In other words, even though it is energetically more favorable for $\mathrm{V}_{\mathrm{O}}^{\bullet\bullet}$ to accompany $\mathrm{Y}_{\mathrm{Zr}}'$ upon segregation to this GB, the magnitude of the driving force is smaller than for the Σ5 (310)/[001] GB.

More widely scattered data were obtained for the Σ13 (510)/[001] GB, as shown in Fig. 3c, due to the variety of coordination environments in the vicinity of the GB as a result of the smaller misorientation angle compared to Σ5 (310)/[001] and Σ5 (210)/[001] GBs. Both positive and negative segregation energies are calculated for $\mathrm{Y}_{\mathrm{Zr}}'$ in the vicinity of the GB, which implies $\mathrm{Y}_{\mathrm{Zr}}'$ will segregate to some specific sites near the GB but not others. When in association with $\mathrm{V}_{\mathrm{O}}^{\bullet\bullet}$ (i.e., $\left(\mathrm{Y}_{\mathrm{Zr}}' \cdot \mathrm{V}_{\mathrm{O}}^{\bullet\bullet}\right)^{\bullet}$), the segregation energy was negative, becoming more so upon approaching the GB plane. Unlike the previous two GBs, the segregation energies vary further in the vicinity of the GB plane as a consequence of the greater structural distortion around the GB. On the other hand, $\mathrm{V}_{\mathrm{O}}^{\bullet\bullet}$ segregation energies also vary widely, with both positive and negative values in the vicinity of the GB while $E_{\mathrm{diff}}^{\mathrm{YV-Y}}$ is always negative. This indicates that although isolated segregation of $\mathrm{V}_{\mathrm{O}}^{\bullet\bullet}$ is possible, similar to $\mathrm{Y}_{\mathrm{Zr}}'$, at this GB, co-segregation of $\mathrm{Y}_{\mathrm{Zr}}'$ and $\mathrm{V}_{\mathrm{O}}^{\bullet\bullet}$ is more energetically favorable in general as indicated by $E_{\mathrm{diff}}^{\mathrm{YV-Y}}$, since it is always negative within the GB region. Larger differences between $E_{\mathrm{seg}}^{\mathrm{V}}$ and $E_{\mathrm{diff}}^{\mathrm{YV-Y}}$ are found when $E_{\mathrm{seg}}^{\mathrm{V}}$ is positive but similar values are found when $E_{\mathrm{seg}}^{\mathrm{V}}$ is negative. This indicates that $\mathrm{V}_{\mathrm{O}}^{\bullet\bullet}$ plays a role in promoting segregation of $\mathrm{Y}_{\mathrm{Zr}}'$, especially when it is energetically unfavorable for it to segregate on its own to this GB; however, the magnitude of the driving force for co-segregation of $\mathrm{V}_{\mathrm{O}}^{\bullet\bullet}$ and $\mathrm{Y}_{\mathrm{Zr}}'$ to favorable sites is not as great as for the Σ5 (310)/[001] GB. Taking this into account, it is expected that oxygen vacancies can move away from the GB leaving the vicinity of the GB enriched with yttrium to increase the entropy when temperature is raised. This would significantly influence conduction of O^{2-} ions along and across the GB, as we showed using molecular dynamics in a previous study [56].

In the case of the Σ9 (221)/[011] GB, the $\mathrm{Y}_{\mathrm{Zr}}'$ segregation energy decreased upon approaching the GB plane, as shown in Fig. 3d. Segregation of $\left(\mathrm{Y}_{\mathrm{Zr}}' \cdot \mathrm{V}_{\mathrm{O}}^{\bullet\bullet}\right)^{\bullet}$ complexes is more energetically favorable, implying $\mathrm{V}_{\mathrm{O}}^{\bullet\bullet}$ is necessary to some extent for $\mathrm{Y}_{\mathrm{Zr}}'$ segregation. Unfortunately, all the results for segregation energy of oxygen vacancies were unphysical: Structural changes triggered by introduction of the vacancy but not directly related to it were produced during structural optimization, resulting in scattered data with differences in segregation energy of as much as 2.0 eV even for the grain interior, i.e., $r > 1.0$ nm. Thus, data for $\mathrm{V}_{\mathrm{O}}^{\bullet\bullet}$ segregation are not shown in the figure. Differences in segregation energies of $\mathrm{Y}_{\mathrm{Zr}}'$ and $\left(\mathrm{Y}_{\mathrm{Zr}}'\cdot\mathrm{V}_{\mathrm{O}}^{\bullet\bullet}\right)^{\bullet}$ were found at $r < 1.1$ nm, a slightly wider region than for other GBs, due to closer packing of ions in the vicinity of this GB.

Finally, although both positive and negative segregation energies are calculated for $\mathrm{Y}_{\mathrm{Zr}}'$ depending on the site near the Σ11 (113)/[011] GB plane, their magnitudes are modest, probably because the energy of this GB is low [57], as shown in Fig. 3d. Those for $\left(\mathrm{Y}_{\mathrm{Zr}}'\cdot\mathrm{V}_{\mathrm{O}}^{\bullet\bullet}\right)^{\bullet}$ complexes are all negative but also not particularly large. Segregation energies for $\mathrm{V}_{\mathrm{O}}^{\bullet\bullet}$ are scattered, with modest segregation energies in the vicinity of the GB plane. The same is true for $E_{\mathrm{diff}}^{\mathrm{YV-Y}}$, indicating that $\mathrm{V}_{\mathrm{O}}^{\bullet\bullet}$ is not needed for segregation of $\mathrm{Y}_{\mathrm{Zr}}'$ to occur, except for the GB core, where $\mathrm{V}_{\mathrm{O}}^{\bullet\bullet}$ shifts from its initial site upon structural optimization because of the relatively larger magnitude of the segregation energy compared to neighboring sites. Thus, of all the GBs examined in this study, $\mathrm{V}_{\mathrm{O}}^{\bullet\bullet}$ segregation has the least effect on $\mathrm{Y}_{\mathrm{Zr}}'$ segregation. However, it should be noted that $\mathrm{V}_{\mathrm{O}}^{\bullet\bullet}$ itself tends to be segregated to the GB, even though the magnitude of the segregation energy is smaller than for other GBs.

So far, only the simplest association of point defects, $\left(\mathrm{Y}_{\mathrm{Zr}}'\cdot\mathrm{V}_{\mathrm{O}}^{\bullet\bullet}\right)^{\bullet}$, has been examined. However, it is reasonable to examine a neutral defect complex, $\left(2\mathrm{Y}_{\mathrm{Zr}}'\cdot\mathrm{V}_{\mathrm{O}}^{\bullet\bullet}\right)^{\times}$, in order to generalize the results further. Figure 4 shows segregation energies of $\left(2\mathrm{Y}_{\mathrm{Zr}}'\cdot\mathrm{V}_{\mathrm{O}}^{\bullet\bullet}\right)^{\times}$ as a function of distance from different GB planes. The segregation energies show similar trends to those for the binary complexes: The defect complex tends to strongly segregate at the Σ5 (210)/[001] GB, while the magnitude of its segregation energy at the Σ5 (210)/[001] GB is smaller. The segregation energies for the neutral defect complex at the Σ13 (510)/[001] GB are somewhat scattered as a result of the variety of coordination environments in the vicinity of the GB mentioned earlier. Segregation of the complex is energetically favorable at the Σ9 (221)/[011] GB, while it appears to be suppressed at the Σ11(113)/[011] GB.

In order to obtain a more general picture of GB segregation in terms of coordination environment, further analyses were carried out. First, segregation energy was plotted as a function of bonding distance or coordination number, but this failed to reveal any general trends, probably because these factors are correlated with each other. Next, we measured the number density of O^{2-} ions on nearest neighbor sites around cations in the vicinity of each GB, d, as follows:

$$d = \frac{\mathrm{CN}}{4/3\cdot\pi\cdot r^{3}} \tag{9}$$

where CN denotes the coordination number of O^{2-} ions around a cation and r is the average distance between a cation and its nearest neighbor O^{2-} ions.

Segregation energies of $\left(2\mathrm{Y}_{\mathrm{Zr}}'\cdot\mathrm{V}_{\mathrm{O}}^{\bullet\bullet}\right)^{\times}$ for the five GBs examined are plotted as a function of d in Fig. 5. This figure clearly shows there is a relationship between these two quantities independent of the GB or its misorientation: When the number density of O^{2-} ions is small or the number density of $\mathrm{V}_{\mathrm{O}}^{\bullet\bullet}$ is large the segregation energy is

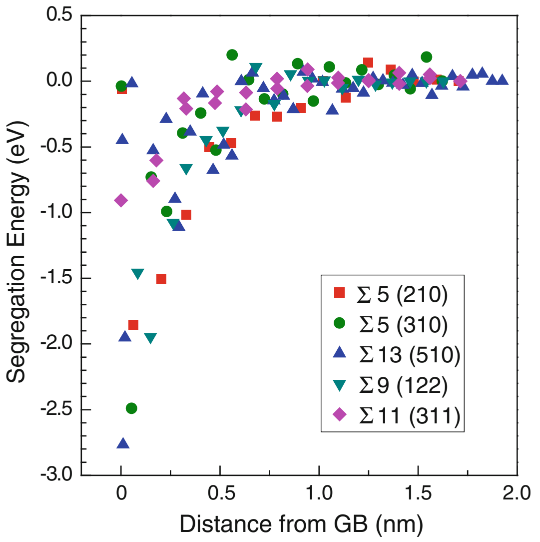

Fig. 4 Segregation energies of a $\left(2\mathrm{Y}_{\mathrm{Zr}}'\cdot\mathrm{V}_{\mathrm{O}}^{\bullet\bullet}\right)^{\times}$ complex for five GBs as a function of distance from the GB plane

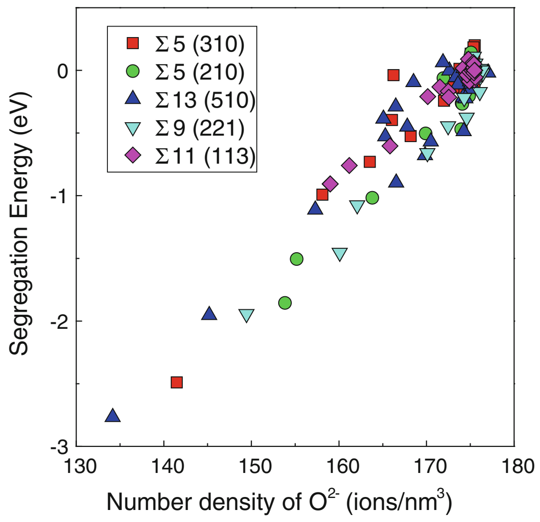

Fig. 5 Relationship between segregation energies of a $\left(2\mathrm{Y}_{\mathrm{Zr}}'\cdot\mathrm{V}_{\mathrm{O}}^{\bullet\bullet}\right)^{\times}$ complex at five GBs and the number density of O^{2-} ions about each cation

small, while the number density of O^{2-} ions is as same as in the bulk where the segregation energy is nearly zero. The range of data varies from GB to GB, however. Since the number density of O^{2-} ions (i.e., the coordination environments) of cations can be directly related to GB energy through Eqs. 2 and 3, this shows that there is a correlation between GB energy, which depends on the coordination environment in the vicinity of a GB, and the segregation energy of the neutral defect complex, as demonstrated in our separate study [56]. Thus, in contrast to the space-charge theory [39], on the atomic level, $V_O^{\bullet\bullet}$ is needed for segregation of Y'_{Zr} to occur, although the degree of segregation will differ from GB to GB, perhaps depending on the GB energy. Based on the range of GBs examined in this study, this finding likely holds irrespective of the misorientation of the grains at a GB. The results presented so far are for infinitely dilute concentrations of impurities and vacancies only. Segregation at higher concentrations also needs to be considered, which is addressed in the next section.

Equilibrium segregation concentrations

Calculations in the previous section were for infinitely dilute concentrations of defects and thus neglected interactions among defect or defect complexes. In order to estimate local equilibrium concentrations of these defects at GBs, interactions between defects need to be taken into account. In this section, local equilibrium defect concentrations within GB regions, i.e., up to 1.0 nm either side of a given GB plane, were evaluated for the five GBs.

Under equilibrium conditions, it is reasonable to assume that the concentrations of Y'_{Zr} and $V_O^{\bullet\bullet}$ in the grain interior are essentially the same as the macroscopic concentrations since the volume fraction of GBs is negligibly small. In the case of nanocrystals, however, the proportion of the GBs increases, so that this assumption is invalidated. At equilibrium, chemical potentials, i.e., the energy change associated with doping, of both regions should be equal:

$$\mu_{GB}(n_Y) = \mu_{GI}(n_Y) \tag{10}$$

where $\mu_{GB}(n_Y)$ and $\mu_{GI}(n_Y)$ are chemical potentials of the GB region and grain interior, respectively, as a function of the number of yttrium ions in the each region, n_Y. From the equilibrium condition, the local concentration of both dopants and vacancies can be evaluated for a given concentration in the grains or the macroscopic concentration. The chemical potential of each region is given by

$$\mu(n_Y) = \mathrm{d}E_{\mathrm{total}}(n_Y)/\mathrm{d}n_Y \tag{11}$$

where $E_{\mathrm{total}}(n_Y)$ is the total energy of a supercell as a function of n_Y. This equation can be approximated as

$$\mu(n_Y) = [E_{\mathrm{total}}(n_Y + 4) - E_{\mathrm{total}}(n_Y - 4)]/8. \tag{12}$$

To calculate chemical potentials according to this equation, total energies of supercells containing $4i$ of yttrium, where i is an integer, or half this number, i.e., $2i$ of $\left(2Y'_{Zr} \cdot V_O^{\bullet\bullet}\right)^{\times}$ complexes, were calculated as a function of Y'_{Zr} content. Since each supercell contains two GBs, the minimum increment for the number of Y'_{Zr} species is four.

To allow for a larger number of defect configurations, the supercells were repeated in the b and c directions so that all lengths were greater than 2.0 nm. Changes of positions of both Y'_{Zr} and $V_O^{\bullet\bullet}$ species were confined to the GB region, i.e., 1.0 nm either side of the GB plane, to reduce the possible number of defect configurations and increase the efficiency of the Monte Carlo simulations. Furthermore, to simulate all five GBs in a reasonable amount of time, the distance between the GBs in each supercell was reduced to minimum of ca. 2.25 nm depending on the convergence of segregation energies shown in Fig. 3. A few simulations were performed with the initial GB separation lengths to confirm that such a reduction did not modify the resulting chemical potentials to a significant degree. Chemical potentials for the bulk (i.e., grain interior) were also evaluated as a function of Y'_{Zr} content [25]. Unfortunately, calculations of total energies for Σ9 (221)/[011] and Σ11(113)/[011] GBs were not accurate enough to obtain chemical potentials by derivation from discrete values especially when the $\left(2Y'_{Zr} \cdot V_O^{\bullet\bullet}\right)^{\times}$ content was increased. Slight structural changes triggered by $\left(2Y'_{Zr} \cdot V_O^{\bullet\bullet}\right)^{\times}$ addition but not directly related to the addition were observed, resulted in unacceptably large uncertainties in the calculated chemical potentials. This instability can be probably attributed to the polarity of the GB planes. Hence in this section we focus only on three GBs, namely Σ5 (210)/[001], Σ5 (310)/[001], and Σ13 (510)/[001] GBs.

Calculated chemical potentials are compared in Fig. 6. Bulk values remain high at around 43.5 eV, almost independent of concentration. In contrast, those for the three GBs are much smaller at low local concentration. This indicates that when a polycrystalline sample is very pure, $\left(2Y'_{Zr} \cdot V_O^{\bullet\bullet}\right)^{\times}$ preferentially segregates at GBs. Chemical potentials of GBs increased with the increase of local concentration of $\left(2Y'_{Zr} \cdot V_O^{\bullet\bullet}\right)^{\times}$ in the GB region and they reach similar values to the bulk value when the local concentration is around 22 at.%. These results indicate that below this concentration all $\left(2Y'_{Zr} \cdot V_O^{\bullet\bullet}\right)^{\times}$ clusters segregate to the GB, leaving the grain interior devoid of defects under equilibrium conditions. At higher concentrations, $\left(2Y'_{Zr} \cdot V_O^{\bullet\bullet}\right)^{\times}$ clusters exist in both grain interiors and GB

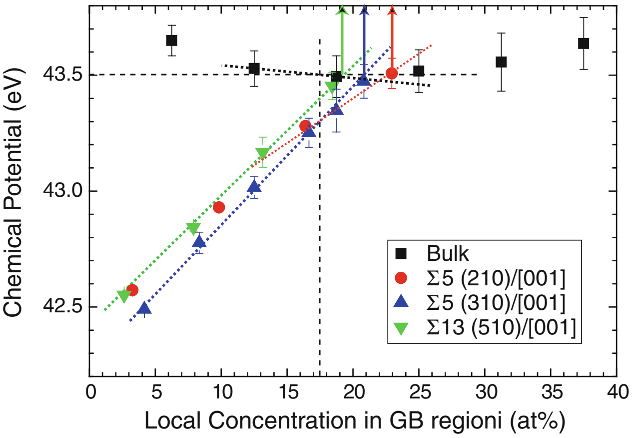

Fig. 6 Chemical potentials for the bulk crystal and Σ5 (210)/[001], Σ5 (310)/[001], and Σ13 (510)/[001] GBs as a function of local concentration of Y'_{Zr}

regions, maintaining a balance between the chemical potentials between the two regions. It should be noted that internal coordinates of the defect cluster were not fixed in these calculations.

Equilibrium local concentrations of defects in GB regions were calculated as follows: First, from the bulk curve, the chemical potential for 9.6 mol% Y_2O_3-doped ZrO_2, containing 17.5 at.% Y'_{Zr}, was determined to be about 43.5 eV by interpolation. Next, the local concentration in the GB region for each GB was determined so that the chemical potential for the local concentration was equal to about 43.5 eV by extrapolating the data. Although the number of data points in this figure is insufficient to obtain very accurate values, equilibrium local concentrations in the GB region of Σ5 (210)/[001], Σ5 (310)/[001], and Σ13 (510)/[001] systems were estimated to be 19, 21, and 23 at.%, respectively. The estimated Y'_{Zr} content for the Σ5 (310)/[001] GB is in good agreement with experiment [6]. It should be noted that the calculated local concentrations vary with the definition of the GB region width, in the case of this study set at 1.0 nm either side of the GB plane. The values for these three GBs vary only slightly from each other, in spite of the difference in the GB structures, the magnitude of the driving force for $V_O^{\bullet\bullet}$ segregation to accompany Y'_{Zr} segregation, and the difference in segregation energies of $\left(2Y'_{Zr} \cdot V_O^{\bullet\bullet}\right)^{\times}$ shown in Fig. 4. Reasons for this may be that: (1) only sites having negative segregation energies at infinitely dilute concentration are occupied upon high-concentration segregation; (2) interaction energies between $\left(2Y'_{Zr} \cdot V_O^{\bullet\bullet}\right)^{\times}$ complexes govern high-concentration segregation; or (3) both of the above. Since it is practically impossible to separate the effects of (1) and of (2), it remains unclear which of these factors governs the segregation behavior at higher dopant concentration. However, taking into account the actual spatial separation between $\left(2Y'_{Zr} \cdot V_O^{\bullet\bullet}\right)^{\times}$ species and the dependence of chemical potential on the local concentration, (3) is the most likely cause of the similar segregation behavior of these three GBs. Nowotny, et al. argued that surface segregation is dependent on the crystallographic orientation of the surface [34], and a similar trend is expected for GB segregation. It is thus worthwhile examining a wider range of GBs with different structures and energies to see if there is any difference in overall equilibrium concentration within GB regions.

In spite of the similar amount of segregation to these three GBs, there are significant changes in atomic configurations at segregated GB compared to undoped GBs, and the spatial distribution of Y'_{Zr} and $V_O^{\bullet\bullet}$ species is also different in each case. Figure 7 compares plots of the atomic coordinates projected onto the (001) plane for the optimized pure ZrO_2 GB, the initial GB with segregated defects, and the optimized GB with segregated defects, for the three GBs. The structure of the pure Σ5 (210)/[001] GB is completely mirror-symmetric about the GB plane. While the half-filled Zr columns indicated in Fig. 2 remain separated even after structural optimization, the half-filled O columns as well as other O columns immediately next to the GB plane are slightly displaced from the ideal (initial) positions, indicating that the potential energy surface for O^{2-} ions is relatively flat. Since the misorientation angle is larger than at other GBs, more free volume is available at this GB. In the initial structure of the GB with segregated defects shown in the middle of Fig. 7a, Y'_{Zr} species are not located just within Zr columns in the GB plane, but instead occupy neighboring columns in a mirror-symmetric manner. After structural optimization of this GB, the mirror symmetry is broken and a glide-type GB is formed as indicated by dotted lines in Fig. 7a. This contrasts with the results of our systematic study of GBs in FCC Al with a [001] rotation axis [55], where the opposite was found: Even if the initial configuration forms a glide-type GB, a mirror-symmetric CSL GB is obtained after structural optimization regardless of the misorientation angle [55]. FCC Al and ZrO_2 contain very different types of bonds; metallic in the former and ionic in the latter. On the other hand, different tendencies are found for Σ5 (310)/[001] GBs. As shown in Fig. 7b, both half-filled Zr columns and O columns remain separate even after structural optimization for pure ZrO_2. The initial distribution of Y'_{Zr} at the GB is neither uniform nor mirror-symmetric. However, structural optimization of this GB yielded a mirror-symmetric atomic configuration at this GB with the pairs of half-filled O columns partially merged and pairs of the half-filled Zr columns now occupied by Y'_{Zr} completely merged. The atomic coordinates at this GB agree quite well

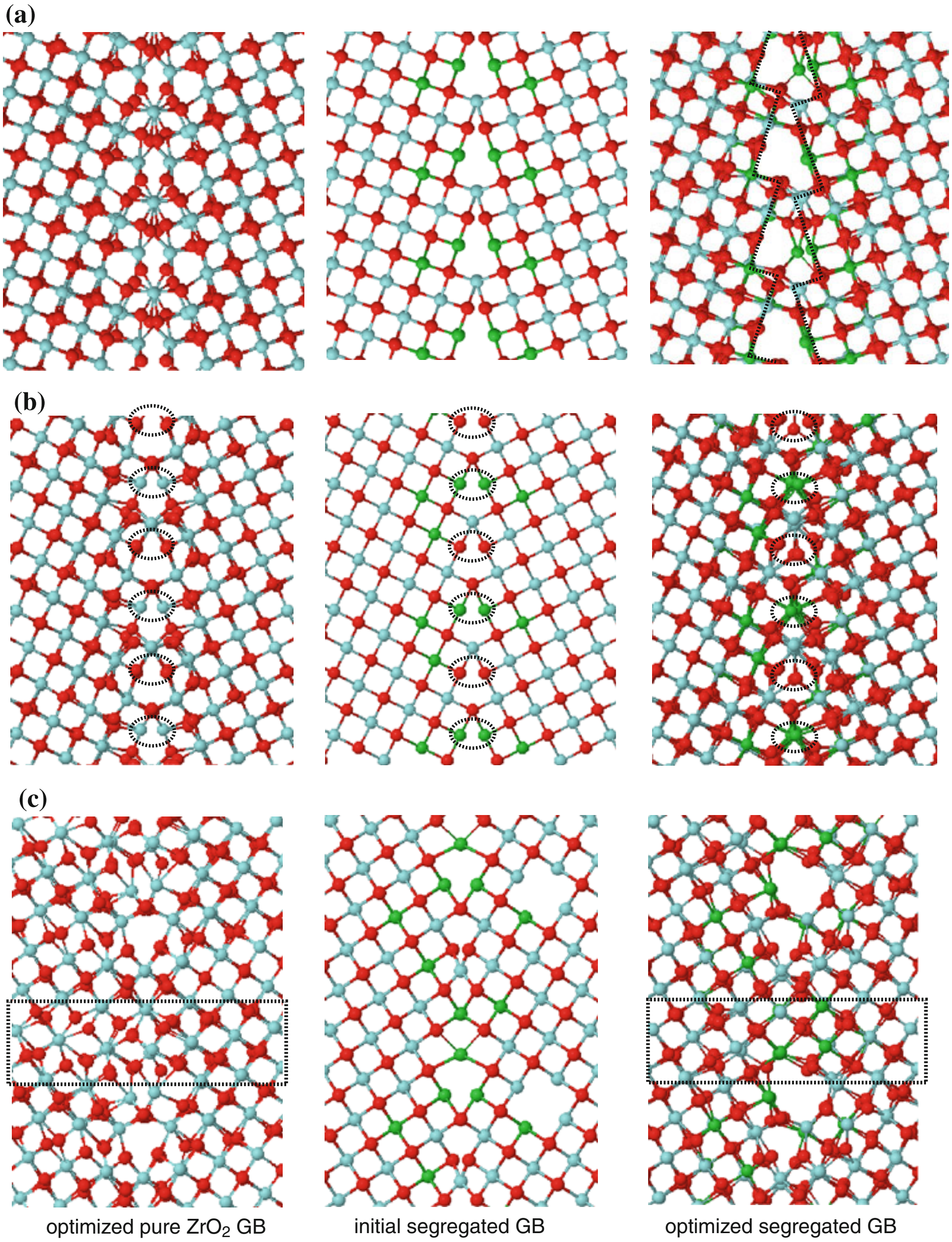

Fig. 7 Magnified images showing atomic coordination projected onto a two-dimensional plane perpendicular to GB planes for optimized pure GBs (*left*), initial structures of GB with segregated dopants (*center*), and optimized structures of GBs with segregated dopants (*right*) for **a** Σ5 (210)/[001], **b** Σ5 (310)/[001], and **c** Σ13 (510)/[001] GBs. *Light blue balls* and *red balls* (*light gray balls* and *dark gray balls* in *gray scale*) represent Zr and O atoms, respectively. *Green balls* (*dark gray balls* on Zr sublattice) represent Y atoms (Color figure online)

with an experimentally obtained Z-contrast image [6], while those for a pure ZrO_2 GB fail to reproduce the Z-contrast image [25]. Finally, the atomic configuration at Σ13 (510)/[001] GBs is more complicated than for the previous two GBs because of the smaller misorientation angle and thus the more closed-packed arrangement of ions near the GB plane. In spite of the mirror-symmetric initial configuration of the pure GB shown in Fig. 3c, structural optimization yielded an asymmetrical configuration about the GB plane, especially in the case of the O columns, as highlighted by the dotted box in Fig. 7c. The distribution of Y'_{Zr} species in the initial structure was also asymmetric, as was the case for the Σ5 (310)/[001] GB, and one of the O columns was completely replaced by vacancies on the right-hand side of the GB plane. After structural optimization, the atomic configuration remained asymmetric, in contrast to the Σ5 (310)/[001] GB, in which the optimized structure was symmetric. The $V_O^{\bullet\bullet}$ column moved toward the GB plane. However, due to the complexity of this GB, atom columns, especially the O columns indicated by the dotted box in Fig. 7c, form a periodic arrangement as a result of segregation of Y'_{Zr} and $V_O^{\bullet\bullet}$; O columns in the dotted box at the GB are well aligned with only small deviations. As a result, a glide-like GB is formed when segregated defects are present, similar to the case of the Σ5 (210)/[001] GB. As mentioned above, the formation of a glide-like atomic configuration at the Σ13 (510)/[001] GB is similar to that at the Σ5 (210)/[001] GB, but is quite different to that in FCC Al; on the other hand, the Σ5 (310)/[001] GB yielded a mirror-symmetric structure like FCC Al. The reason for this difference is not immediately apparent. The structure of the Σ5 (310)/[001] GB is less distorted both with and without defect segregation than the other GBs. This might be the reason for the difference in GB structures with segregated defects in relation to the mirror symmetry. However, it should be noted that GB segregation of Y'_{Zr} and $V_O^{\bullet\bullet}$ at Σ5 (210)/[001] or Σ13 (510)/[001] GBs helps the crystal lattice to return to its original (bulk-like) configuration, even immediately next to the GB plane, instead of forming kite-shaped structural units at the GB core that typify the distorted structures at pure GBs.

Since it is difficult to understand the spatial distribution of both Y'_{Zr} and $V_O^{\bullet\bullet}$ defects from the two-dimensional projected images shown in Fig. 7, the distribution of each element in the GB region was plotted in one dimension after broadening using a Gaussian function with full-width at half-maximum (FWHM) of 0.05 nm to produce Fig. 8. The overall distributions of Y'_{Zr} are similar to each other and converge to zero at around 0.6 nm, well within the GB region width defined in this study. They are asymmetric about the GB plane for Σ5 (210)/[001] and Σ13 (510)/[001] GBs, reflecting the asymmetric atomic configurations in the vicinity of the GBs. The distribution of Y'_{Zr} for the Σ5 (310)/[001] GB is also slightly asymmetric about the GB plane, although the atomic coordination is symmetric. The number density of Y'_{Zr} at the Σ5 (210)/[001] GB is the highest and that of Σ13 (510)/[001] is the lowest among these three GBs.

The deviation in the O distribution across GBs compared to that in the bulk was found to occur over a wider region than for Y'_{Zr}, irrespective of the GB misorientation, almost extending to the edge of the GB region. This implies that widening the GB region in the calculations might change the distribution of O across GBs. This is likely to be the case at higher temperature, since $V_O^{\bullet\bullet}$ is mobile, while the diffusivities of Zr and Y ions are many orders of magnitude lower. Although this is beyond the scope of this study, we address this issue in a molecular dynamics study of ionic conduction in ZrO_2 [56]. In the current low-temperature case, the $V_O^{\bullet\bullet}$ distribution is narrower at the Σ5 (310)/[001] GB than at the other two GBs, consistent with the larger driving force for $V_O^{\bullet\bullet}$ segregation to accompany Y'_{Zr} segregation at this GB. The $V_O^{\bullet\bullet}$ distribution is wider at the Σ13 (510)/[001] GB than the Σ5 (210)/[001] GB probably because the Σ13 (510)/[001] GB is more distorted as a result of the high atom density associated with a smaller misorientation angle. Although the defect distributions at the Σ (510)/[001] GB are similar to that predicted by space-charge theory [39], the distributions at the Σ5 (310)/[001] GB are completely different since the oxygen vacancies are more strongly segregated to the GB.

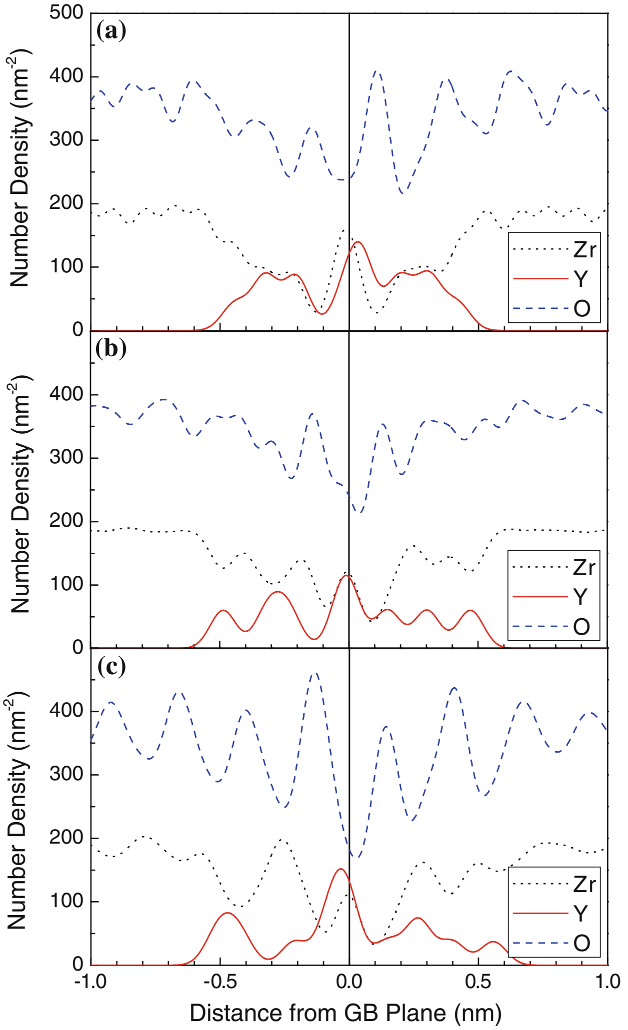

Fig. 8 Spatial distribution of Zr, Y, and O atoms across GB planes using a Gaussian function with full-width at half-maximum of 0.05 nm: **a** Σ5 (210)/[001], **b** Σ5 (310)/[001], and **c** Σ13 (510)/[001] GBs

Finally, based on the three-dimensional configuration of Y'_{Zr} at different GBs, the fraction of Y that can be measured by elemental analysis was calculated as a function of spatial resolution by assuming that the measuring probe was centered on the GB plane (Fig. 9). It is noted that a slight depletion of Y'_{Zr} can be observed at GB cores of Σ5 (210)/[001] and Σ13 (510)/[001] GBs when the spatial resolution is better than a few Ångstroms. However, when the spatial resolution is around 1.0 nm, distinguishing

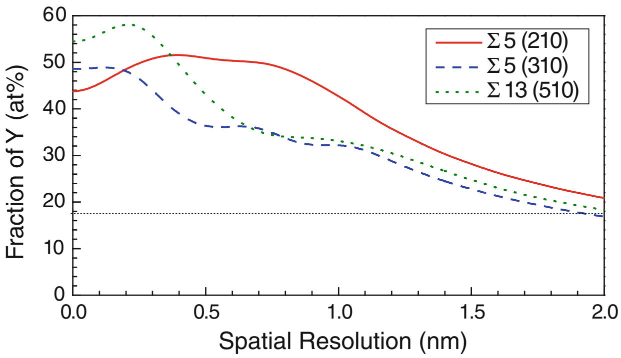

Fig. 9 Calculated Y fractions for Σ5 (210)/[001] (*red solid curve*), Σ5 (310)/[001] (*blue broken curve*), and Σ13 (510)/[001] (*green dotted curve*) GBs as a function of spatial resolution centered on the GB plane. The *black dotted line* corresponds to the Y fraction in the bulk crystal of 9.6 mol% Y_2O_3-doped ZrO_2 (Color figure online)

between Σ5 (310)/[001] and Σ13 (510)/[001] GBs is almost impossible.

Summary

Static lattice calculations on the atomic level were carried out to determine segregation energies of point defects or defect complexes at infinitely dilute concentration in Y_2O_3-doped ZrO_2. Although segregation of Y'_{Zr} varies with the coordination environments at GBs, it is more energetically favorable when accompanied by $V_O^{\bullet\bullet}$ segregation, with the amount of $V_O^{\bullet\bullet}$ required for stabilization varying from GB to GB. Based on analyses of $\left(2Y'_{Zr} \cdot V_O^{\bullet\bullet}\right)^{\times}$ defect complexes, it was found that the segregation energy is correlated to the coordination environment, and, in turn, GB energy. Atomistic simulations of higher defect concentrations at three different GBs revealed similar equilibrium concentrations of defects in the vicinity of the GB, perhaps because they have similar GB energies, although the precise distribution of defects, especially $V_O^{\bullet\bullet}$, differs for each GB, which would affect O^{2-} ion conduction along or across these interfaces. The driving force for GB segregation was revealed to be minimization of stresses induced by distortion of the crystal lattice at the discontinuity (i.e., GB).

Acknowledgements The authors are grateful for useful discussions with Drs H. Matsubara and C. A. J. Fisher at the Japan Fine Ceramics Center and Prof. K. Matsunaga at Kyoto University. This study is in part supported by Grant-in-Aid for Scientific Research on Priority Areas “Atomic Scale Modification” (No. 474) from the Ministry of Education, Culture, Sports, Science and Technology, Japan.

References

1. Hondros ED, Seah MP (1983) In: Cahn RW, Haasen P (eds) Physical metallurgy. Amsterdam, North-Holland
2. Hondros ED, Seah MP (1977) Metal Trans A 8:1363
3. Hofmann S (1987) J Chim Phys Phys Chim Biol 84:141
4. Sutton AP, Balllufi RW (1995) Interfaces in crystalline materials. Oxford University Press, New York
5. Ikuhara Y, Thavorniti P, Sakuma T (1997) Acta Mater 45:5275
6. Dickey EC, Fan X, Pennycook SJ (2001) J Am Ceram Soc 84:1361
7. Shibata N, Morishige N, Yamamoto T, Ikuhara Y, Sakuma T (2002) Philos Mag Lett 82:175
8. Shibata N, Yamamoto T, Ikuhara Y, Sakuma T (2001) J Electron Microsc 50:429
9. Shibata N, Oba F, Yamamoto T, Ikuhara Y (2004) Philos Mag 84:2381
10. Nohara Y, Tochigi E, Shibata N, Yamamoto T, Ikuhara Y (2010) J Electron Microsc 59:S117
11. Backhaus-Ricoult M, Badding M, Thibault Y (2006) Ceram Trans 179:173
12. Hertz JL, Rothschild A, Tuller HL (2009) J Electroceram 22:428
13. Fergus JW (2006) J Power Sources 162:30
14. Ormerod RM (2003) Chem Soc Rev 32:17
15. Fleming WJ (1977) J Electrochem Soc 124:21
16. Verkerk MJ, Middlehuis BJ, Burggraaf AJ (1982) Solid State Ionics 6:159
17. Fisher CAJ, Matsubara H (1999) J Eur Ceram Soc 19:703
18. Cheikh A, Madani A, Touati A, Boussetta H, Monty C (2001) J Eur Ceram Soc 21:1837
19. Chun SY, Mizutani N (2001) Appl Surf Sci 171:82
20. Nakagawa T, Sakaguchi I, Shibata N, Matsunaga K, Yamamoto T, Haneda H, Ikuhara Y (2005) J Mater Sci 48:3185. doi: 10.1007/s10853-005-2682-4
21. Peters C, Weber A, Gerthsen D, Ivers-Tiffée E (2009) J Am Ceram Soc 92:2017
22. Hughes AE, Sexton BA (1989) J Mater Sci 24:1057. doi: 10.1007/BF01148798
23. Nieh TG, Yaney DL, Wadsworth J (1989) Scripta Mater 23:2007
24. Boulc’h F, Djurado E, Dessemond L (2004) J Electrochem Soc 151:A1210
25. Oyama T, Yoshiya M, Matsubara H, Matsunaga K (2005) Phys Rev B 71:224105-1
26. Matsui K, Yoshida H, Ikuhara Y (2008) Acta Mater 56:1315
27. Zapata-Solvas E, de Bernardi-Martín S, Gómez-García D (2010) Int J Mater Res 101:84
28. Chaim R, Brandon DG, Heuer AH (1986) Acta Metall 34:1933
29. Whalen PJ, Reidinger F, Correale ST, Marti J (1987) J Mater Sci 22:4465. doi:10.1007/BF01132048
30. Theunissen GSAM, Winnubst AJA, Burggraaf AJ (1989) J Mater Sci Lett 8:55
31. Hughes AE, Badwal SPS (1990) Solid State Ionics 40(41):312
32. Hughes AE, Badwal SPS (1991) Solid State Ionics 46:265
33. Stanek CR, Grimes RW, Rushton MJD, McClellan KJ, Rawlings RD (2005) Philos Mag Lett 85:445
34. Nowotny J, Sorrell CC, Bak T (2005) Surf Interface Anal 37:316
35. Wang XG (2008) Surf Sci 602:L5
36. Lahiri J, Mayernick A, Morrow SL, Koel BE, van Duin ACT, Janik MJ, Batzill M (2010) J Phys Chem C 114:5990
37. Mayernick AD, Batzill M, van Duin ACT, Janik MJ (2010) Surf Sci 604:1438
38. Lee HB, Prinz FB, Cai W (2010) Acta Mater 58:2197
39. Guo X (1995) Solid State Ionics 81:235
40. Guo X, Maier J (2001) J Electrochem Soc 148:E121
41. Guo X, Zhang Z (2003) Acta Mater 51:2539
42. Guo X, Ding Y (2004) J Electrochem Soc 151:J1
43. De Souza RA, Pietrowski MJ, Anselmi-Tamburini U, Kim S, Munir ZA, Martin M (2008) Phys Chem Chem Phys 10:2067
44. Durá OJ, López de la Torre MA, Vázquez L, Chaboy J, Boada R, Rivera-Calzada A, Santamaria J, Leon C (2010) Ionic

conductivity of nanocrystalline yttria-stabilized zirconia: Grain boundary and size effects. Phys Rev B 81:184301-1-9
45. Mondal P, Klein A, Jaegermann W, Hahn H (1999) Solid State Ionics 118:331
46. Knöner G, Reimann K, Röwer R, Södervall U, Schaefer HE (2003) PNAS 100:3870
47. Kosacki I, Rouleau CM, Becher PF, Bentley J, Lowmdes DH (2004) Electrochem Solid-State Lett 7:A459
48. Kosacki I, Rouleau CM, Becher PF, Bentley J, Lowndes DH (2005) Solid State Ionics 176:1319
49. Garcia-Barriocanal J, Rivera-Calzada A, Varela M, Sefrioui Z, Iborra E, Leon C, Pennycook SJ, Santamaria J (2008) Science 321:676
50. Kushima A, Yildiz B (2010) J Mater Chem 20:4809
51. Minervini L, Zacate MO, Grimes RW (1999) Solid State Ionics 116:339
52. Minervini L, Grimes RW, Sickafus KE (2000) J Am Ceram Soc 83:1873
53. Gale JD (1997) J Chem Soc Faraday Trans 93:629
54. Metropolis N, Rosenbluth AW, Rosenbluth MN, Teller AH, Teller E (1953) J Chem Phys 21:1087
55. Yoshiya M, Yoshizu H (2010) Mater Trans 51:51
56. Yoshiya M, Shimizu K, Oyama T, Yasuda H (in preparation)
57. Oyama T, Wada N, Takagi H, Yoshiya M (2010) Phys Rev B 82:134107-1